PHYSICAL REVIEW E **84**, 046402 (2011)

Gold charge state distributions in highly ionized, low-density beam plasmas

M. J. May,[1] S. B. Hansen,[2] J. Scofield,[1] M. Schneider,[1] K. Wong,[1] and P. Beiersdorfer[1]
[1]*PO Box 808 L260, Lawrence Livermore National Laboratory, Livermore California 94551, USA*
[2]*Sandia National Laboratories, ICF Target Design, Albuquerque New Mexico, 87185-1186, USA*

(Received 25 February 2011; revised manuscript received 27 June 2011; published 5 October 2011)

We present a systematic study of Au charge state distributions (CSDs) from low density, nonlocal thermodynamic equilibrium plasmas created in the Livermore electron beam ion traps (EBIT-I and EBIT-II). X-ray emission from Ni-like to Kr-like Au ions has been recorded from monoenergetic electron beam plasmas having $E_{\text{beam}} = 2.66$, 2.92, 3.53, and 4.54 keV, and the CSDs of the beam plasmas have been inferred by fitting the collisionally excited line transitions and radiative recombination emission features with synthetic spectra. We have modeled the beam plasmas using a collisional-radiative code with various treatments of the atomic structure for the complex M- and N-shell ions and find that only models with extensive doubly excited states can properly account for the dielectronic recombination (DR) channels that control the CSDs. This finding would be unremarkable for plasmas with thermal electron distributions, where many such states are sampled, and the importance of DR is well established. But in an EBIT source, the beam is resonant with only a subset of such states having spectator electrons in orbitals with high principal quantum number n ($8 \leqslant n \leqslant 20$). The inclusion of such states in the model was also necessary to obtain agreement with observed stabilizing transitions in the x-ray spectra.

DOI: 10.1103/PhysRevE.84.046402 PACS number(s): 52.20.Fs, 52.25.Jm, 34.70.+e

I. INTRODUCTION

Predicting the correct charge state distribution (CSD) is critical for understanding radiation losses, energy deposition, and energy balance of high-temperature plasmas such as those produced inside Z-pinches [1,2], tokamaks [3,4], astrophysical objects [5], and hohlraums irradiated by intense lasers [6,7]. Accurate models are also necessary for reliable diagnostics of such plasmas. However, the collisional-radiative models that calculate charge state distributions of complex, many-electron ions in nonlocal thermodynamic equilibrium (NLTE) plasmas are, so far, not generally adequate to predict CSDs, particularly far from closed-shell ions. The challenge of such complex systems has been illustrated in comparisons of NLTE calculations for a variety of elements at the NLTE code comparison workshops [8–12]. Calculations for high-Z elements (e.g., Au) for the conditions of typical laser-produced plasmas have had the most significant discrepancies.

Several definitive experiments [13–17] have inferred the CSD of Au in various well-characterized plasmas, mostly laser-produced at moderately high densities. At the NOVA laser, Foord *et al.* [13] inferred the steady-state CSD of a heated gold microdot buried in a Be foil at $n_e = 6 \times 10^{20}$ cm^{-3} and $T_e = 2.2$ keV by comparing the measured $5f \rightarrow 3d$ spectrum with atomic physics calculations. The experimental average ionization state, $\langle q \rangle = +49.3 \pm 0.5$, was in reasonable agreement with the modeled value of +49.1 from RIGEL [18]. To properly reproduce the experiment, two-electron processes such as dielectronic recombination (DR) were included in the modeling of the charge state distribution and the line intensities. More recently at the OMEGA Laser Facility [19], Heeter *et al.* [16,17] determined the charge state distribution of well-characterized NLTE gold plasmas with and without external radiation fields at electron densities near 10^{21} cm^{-3} and at various electron temperatures spanning the range from 0.8 to 2.4 keV. Time- and space-resolved M-shell gold emission spectra were analyzed using a collisional-radiative model with a hybrid level structure (SCRAM) [20], finding average charge states $\langle q \rangle$ ranging from 42 to 50. At lower temperatures (∼165 eV), the spectra included emission features from complex N-shell ions and exhibited significant sensitivity to external radiation fields.

These experiments have provided valuable benchmark data against which to test NLTE codes, since significant discrepancies between codes still persist. Much of the disagreement among codes is thought to be attributable to differing treatments of DR, as evidenced by the results of the NLTE-6 workshop [21], where almost all submitted calculations for cases that artificially excluded DR and Auger processes were in quite good agreement—even for complex, midshell ions. Clearly, experiments at a variety of conditions are needed to test the implementation of the atomic physics processes in the models, and DR and Auger processes are of particular interest. Low-density electron beam ion trap (EBIT) plasmas offer an attractive test bed for this investigation, since the experiments are less complicated than those at high density, with little or no gradients or transient effects. In addition, fewer processes are relevant (e.g., no photoionization, opacity, or three-body recombination). Indeed, dielectronic recombination itself has been generally taken to be of little importance in monoenergetic sources, since it is a resonance process requiring a particular beam energy to capture an electron into and excite an electron from a state in the initial ion, thus forming a doubly excited state in the recombined ion.

In this paper, we demonstrate that DR is a critical process in determining the CSD even for beam plasmas, requiring that extensive atomic structure be included in the models to ensure that the resonance processes are adequately represented in the calculations. We present a systematic and significantly improved set of calculations of CSDs and compare them with experimental CSDs measured from steady-state low-density gold plasmas that were created in the Livermore EBIT-I and EBIT-II electron beam ion traps [22,23]. The majority of the data presented here were taken between 2001 and 2003. The detailed analysis of the spectral line emission has been presented in a previous work [24]. Here, a thorough analysis of the experimentally inferred CSDs from that data is presented for plasmas having monoenergetic electron beam distributions. These beam plasmas had beam energies E_{beam} of 2.66 ± 0.04, 2.92 ± 0.04, 3.53 ± 0.04, and 4.54 ± 0.04 keV and electron densities of $\approx 10^{12}$ cm^{-3}. The predominant ions observed in these plasmas were from Ni-like to Kr-like Au. The CSDs in these beam plasmas were inferred from collisionally excited x-ray line intensities of the $5f \rightarrow 3d$ and $4f \rightarrow 3d$ transitions recorded by photometrically calibrated spectrometers. The recorded spectra were fit with synthetic spectra [25] from the Hebrew University Lawrence Livermore Atomic Code (HULLAC) [26] to determine the CSDs. Additionally, the CSDs in the beam plasmas were inferred by fitting the radiative recombination (RR) emission with calculations from the General Relativistic Atomic Structure Program (GRASP) [27]. The experimentally inferred CSDs and $\langle q \rangle$ values from both methods were consistent for a given plasma condition. The CSDs are in the steady state and in NLTE with no transient conditions.

The CSDs of the plasmas were simulated by Spectroscopic Collisional-Radiative Atomic Model (SCRAM) [20] using atomic physics from Flexible Atomic Code (FAC) [28,29] supplemented by hydrogenic data [30]. The simulations included collisional ionization (CI), RR, excitation autoionization (EA), and DR. Several different simulations were done that had different treatments of DR: two included DR into high-n states using broadened hydrogenic superconfigurations [30]; one of these replaced the hydrogenic states for several of the most critical high-n DR channels with detailed configurations from FAC; and the third model excluded DR into high-n states entirely. The model that excluded DR did not match the CSDs of any of the beam plasmas, predicting CSDs that were more ionized than those recorded in the observed EBIT plasmas. Only the models that included extensive structure in high-n states (e.g., $6fnl(n = 9$ to $15)$ for $E_{\text{beam}} = 3.53$ keV plasmas) were able to reproduce the data with any fidelity. The hybrid-structure approach of the SCRAM model was essential in developing computationally tractable models with the required completeness in the critical high-n DR channels.

II. EXPERIMENT

The gold plasmas used for the present analysis of charge state distributions were created in EBIT-I and EBIT-II between 2001 and 2003. A thorough analysis of the spectral line emission is given in Ref. [24]. The CSDs for the monoenergetic electron beam plasmas under study had beam energies E_{beam} of 2.66 ± 0.04, 2.92 ± 0.04, 3.53 ± 0.04, and 4.54 ± 0.04 keV. The reported beam energies are corrected for the space charge effects of a beam current of ≈ 55 mA [22]. The electron beam had a Gaussian electron energy distribution with a full width half maximum (FWHM) of ≈ 50 eV. In the trap, the gold was ionized by the monoenergetic electron beam. The time history of the Au x-ray emission was monitored with a solid-state Ge detector to check when it came into steady state, which was after 1 second. The ions were held in the trap by the monoenergetic beam for another 8 to 12 seconds for the spectral measurements. The trap was then emptied by removing the voltage on the upper drift tube. For each of the beam energies, the trapping cycle was repeated for a total data acquisition time of ≈ 12 hours, during which time the spectra were recorded. This time was necessary to collect sufficient signal on the spectrometers. Only the data in the steady state portion of the trapping cycle were used for the CSD analysis. In the sections below, the CSDs derived from the RR emission and detailed line spectra from the monoenergetic beam plasmas are presented and compared with SCRAM simulations.

The x-ray crystal spectrometer [31] recorded, in first order and at high resolution, spectra of the $5f \rightarrow 3d$ and the $4f \rightarrow 3d$ transitions of Ni-like to Kr-like gold ions between photon energies of 3100 to 3500 eV and 2400 to 2600 eV, respectively. The design of the x-ray crystal spectrometer accommodated two channels, each having a separate crystal and gas flow proportional counter which allowed both spectral ranges to be measured simultaneously. For these measurements, two Si(111) crystals with lattice spacings of $2d = 6.2712$ Å were used. The nominal Bragg angle was 36° for the $5f \rightarrow 3d$ transitions and 53° for the $4f \rightarrow 3d$ transitions. The x-rays from each crystal were dispersed onto one of the two position-sensitive, gas flow proportional counters filled with ≈ 1 atm of P10 gas. The gas counter windows were either 4 μm of polypropylene or 1 μm of polyimide [32]. In addition, each window was coated with a 100–200 Å Al layer. A vacuum isolation window composed of 0.5 μm of polyimide was located between the crystal spectrometer and EBIT-I or EBIT-II. The total energy coverage of each channel was ≈ 500 eV for the $5f \rightarrow 3d$ transitions and ≈ 300 eV for the $4f \rightarrow 3d$ transitions. The energy resolution was ≈ 5.0 eV at 3300 eV and ≈ 2.5 eV at 2500 eV. A sharp falloff in the efficiency in the higher-energy spectrum occurred below 3210 eV due to the Ar K absorption edge in the P10 gas. The absorption of the gas and the transmission efficiency of the windows were taken into account when the experimental spectrum was compared with the modeling. The crystal spectrometer data were taken using the event mode system [33]. The spectra from the non-steady-state portions of the trapping cycle were filtered out from the final spectra used for the analysis.

An x-ray spectrometer (XRS) microcalorimeter [34,35] from the NASA Goddard Space Flight Center was used to record gold spectral line emission from 1500 to 5000 eV and RR spectra between 4500 and 8000 eV. Details of the XRS photometric calibration are given in [24]. The XRS detector head used for these experiments consisted of an array of 36 ion-implanted thermistors (30 active) with a 8.5 μm-thick HgTe photon absorber, and the total effective area was 12.5 mm^2. Since each absorber-thermistor must recool after each photon event, the maximum count rate was limited to ≈ 100 counts per second across the entire array. This count rate is well suited for the photon fluxes from EBIT-I and EBIT-II plasmas, which are typically low. To keep the total flux onto the XRS below the saturation point, the beam current was kept below 60 mA for these plasmas. The width of the observed lines was ≈ 12 eV. The XRS has an event mode system similar to the one used for the crystal spectrometer.

III. ATOMIC MODELING

In the present work, the hybrid-structure collisional radiative code SCRAM was used to generate both synthetic spectra and the synthetic CSDs for each of the monoenergetic beam

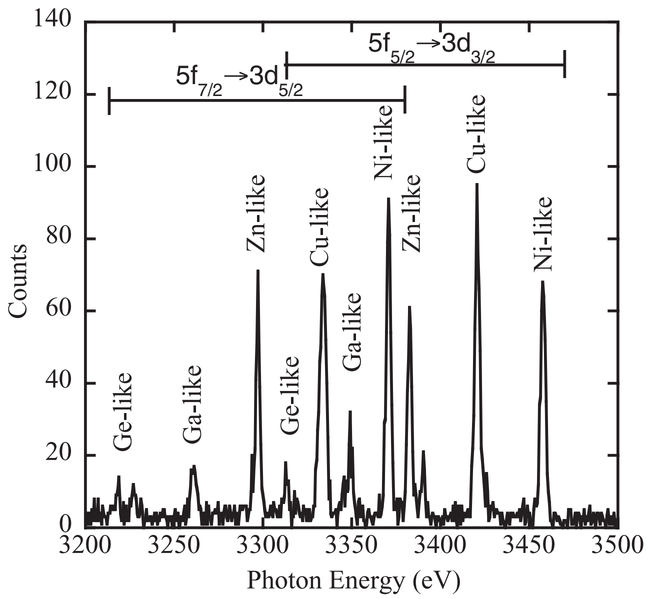

FIG. 1. Raw $5f \rightarrow 3d$ spectrum at an electron beam energy of 3.53 keV recorded with the x-ray crystal spectrometer.

plasma conditions. SCRAM is based on a combination of fine-structure levels for singly excited states and relativistic configurations for high-n and multiply excited states, with both types of states calculated and coupled with rates obtained from the FAC code. Configuration interaction and non-jj-coupling effects are extended from transitions among the fine-structure levels to the unresolved transition arrays (UTAs) among the configurations, ensuring accurate wavelengths and intensities for both resonance lines and satellite features. [36] SCRAM can also be run with an extensive set of hydrogenic superconfigurations (SCs) to ensure statistically complete models; that is, models whose predictions do not change upon addition of more extensive atomic structure. The supplemental SCs incorporate nonzero energy spreads, as described in Ref. [30], to mock up a real distribution of many individual energy levels. This SC broadening is critical for obtaining reasonable CSDs in beam plasmas since, without either broadening of statistically extensive autoionization states or exhaustive calculation of zero-width fine-structure states, any resonance

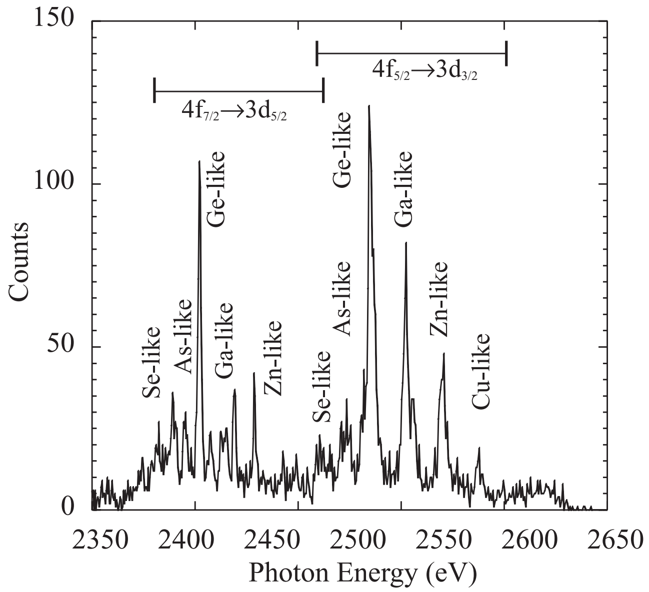

FIG. 2. Raw $4f \rightarrow 3d$ spectrum at an electron beam energy of 2.92 keV recorded with the x-ray crystal spectrometer.

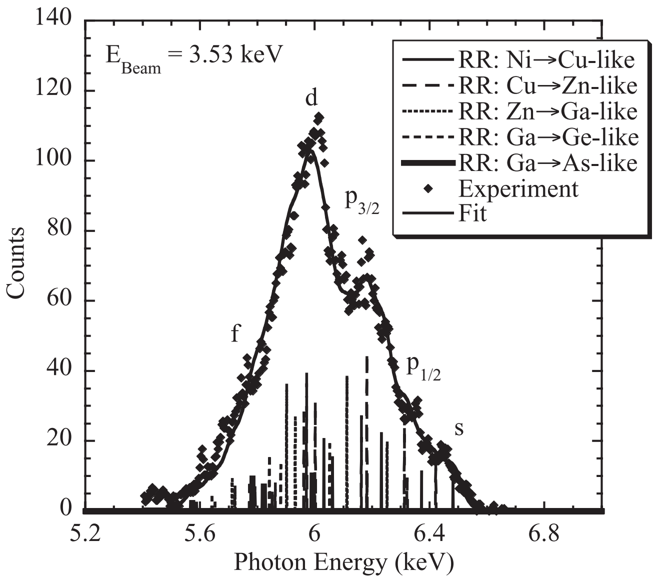

FIG. 3. Radiative recombination spectrum measured by the XRS in a plasma with an $E_{\text{beam}} = 3.53$ keV. The RR features are fit with calculations from GRASP to infer the CSD.

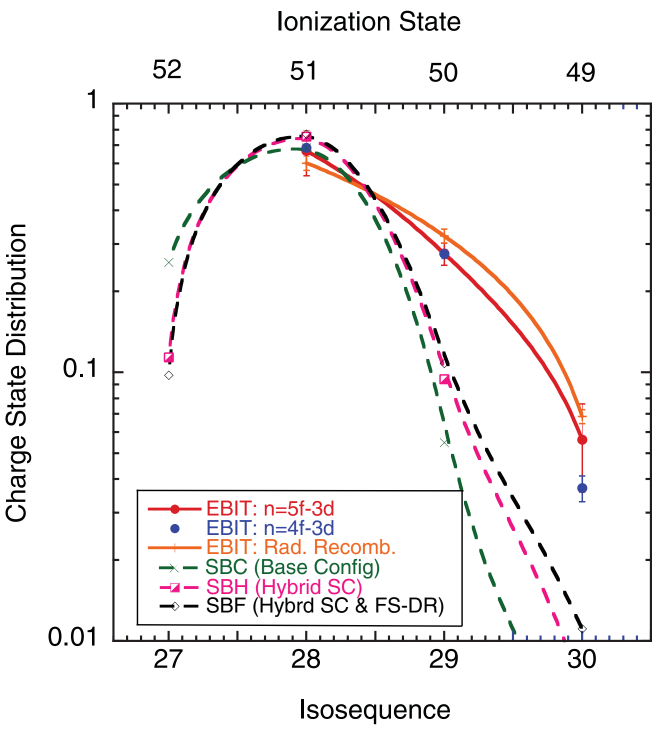

FIG. 4. (Color online) Comparison of the Au charge state distribution at 4.54 keV determined from the $5f \rightarrow 3d$ and $4f \rightarrow 3d$ transitions and radiative recombination emission measured from the EBIT plasma and simulations from SCRAM.

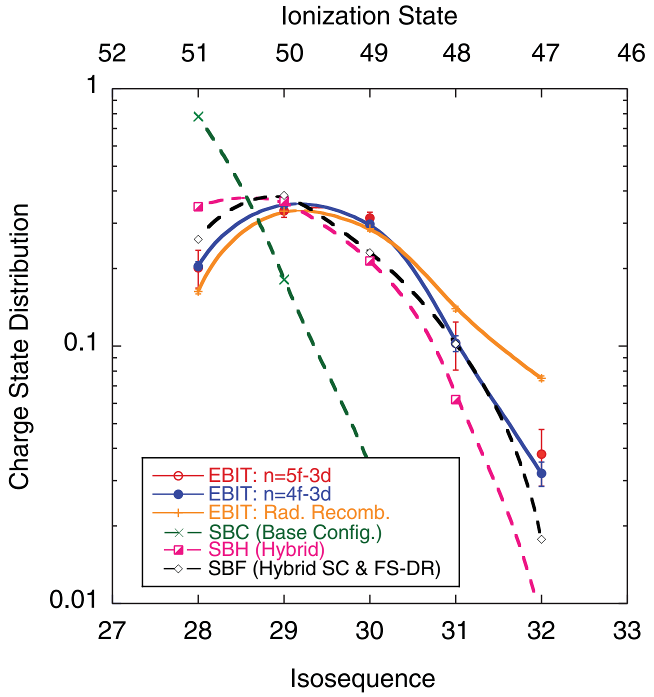

FIG. 5. (Color online) Comparison of the Au charge state distribution at 3.53 keV determined from the $5f \rightarrow 3d$ and $4f \rightarrow 3d$ transitions and radiative recombination emission measured from the EBIT plasma and simulations from SCRAM.

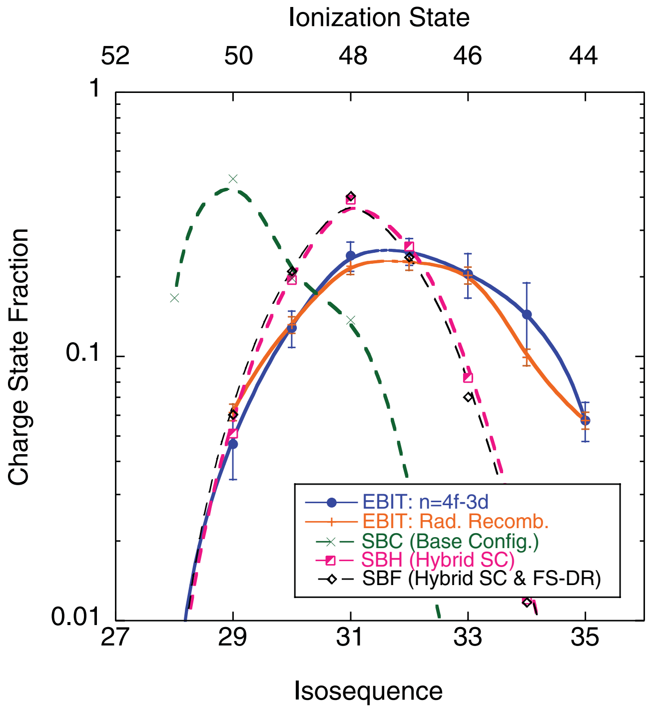

FIG. 6. (Color online) Comparison of the Au charge state distribution at 2.92 keV determined from the $4f \rightarrow 3d$ transitions and radiative recombination emission measured from the EBIT plasma and simulations from SCRAM.

of the DR process with the monoenergetic beam electrons is fortuitous.

The present extended atomic model includes ions from H-like to Kr-like Au, each with single excitations from the valence and inner shell to $n = 20$ and double excitations from the valence and first inner shell to $(n,n') = (10,20)$. The fine-structure levels and relativistic configurations generally only go up to $n = 6$ or 7, with the rest of the structure supplied by the hydrogenic SCs. This model has $\sim 10^6$ levels, which exceeds the memory constraints on many computers. Therefore, a "window" of only 10–20 ions is selected and the hybrid structure is further averaged within SCRAM before the collisional-radiative rate matrix is solved. In this averaging, fine-structure and relativistic configurations are retained in the ground superconfigurations but all other levels are averaged into nonrelativistic configurations. This cuts down the number of levels in the solver to $\sim 10^4$. All of the rates are computed individually and averaged to obtain a $10^4 \times 10^4$ rate matrix that is solved for the averaged level populations. Before constructing synthetic spectra, SCRAM uses these averaged level populations and stored rates between SCs and the levels of the original hybrid model to obtain better-than-statistical populations for the original set of hybrid-structure levels. Each level in each non-ground SC is populated according to the populations of the ground SCs in its own ion and its neighbors multiplied by their total rates into the original hybrid-model level, roughly following the procedure given in [37]. This procedure recaptures the nonstatistical character of levels that were averaged prior to solving the rate matrix.

SCRAM uses atomic structure and transition rates calculated using the FAC atomic data package [28,29]. FAC calculates energy level structures from the Dirac equation with a parametric potential and provides radiative transition and autoionization rates along with collisional excitation, collisional ionization, and photoionization cross sections, which are integrated over the electron and photon distribution functions to obtain direct rates coupling the energy levels. Reverse rates of three-body recombination, radiative recombination, and dielectronic capture are calculated using detailed balance. The supplemental hydrogenic energy levels and the rates coupling them to the rest of the model are computed roughly following [38].

The GRASP [27] package used to simulate the RR features for comparison with the spectra recorded by the XRS from the beam plasmas is an atomic structure code that determines the bound-state radial wave functions by numerically solving the multiconfiguration Dirac-Fock functions. Modifications of the code [39] produce the matrix elements and the cross sections for the continuum processes of RR. GRASP provides cross sections that account for the polarization effects in our EBITs.

IV. CHARGE STATE DISTRIBUTION ANALYSIS

The CSD for each of the monoenergetic beam plasma conditions was determined experimentally by using two different methods. The first method inferred the CSD from the intensity of bound-bound collisionally excited emission lines. The second method inferred the CSD from the free-bound radiative recombination emission.

For the first method, the collisionally excited $5f \rightarrow 3d$ and $4f \rightarrow 3d$ emission lines recorded by the crystal spectrometers were used to infer the CSD. The fractional charge balance

TABLE I. Average $\langle q \rangle$ from calculation and measurement for each beam energy.

	E_{beam}			
	4.54 keV	3.53 keV	2.92 keV	2.66 keV
Source	$\langle q \rangle$	$\langle q \rangle$	$\langle q \rangle$	$\langle q \rangle$
EBIT $5f \rightarrow 3d$	50.7 ± 1.4	49.8 ± 1.4		
EBIT $4f \rightarrow 3d$	50.5 ± 1.0	49.8 ± 0.7	47.1 ± 1.6	46.5 ± 0.8
Line Transition Average	50.6 ± 0.9	49.8 ± 0.8	47.1 ± 1.6	46.5 ± 0.8
EBIT: RR	50.5 ± 1.0	49.4 ± 0.3	47.1 ± 1.0	
SCRAM (Base Config) SBC	51.2	50.4	49.7	48.8
SCRAM (Hybrid SC) SBH	51.1	50.0	47.9	46.5
SCRAM (Hybrid SC + FS-DR) SBF	51.2	49.8	47.9	46.7

was determined by fitting synthetic line brightnesses from the HULLAC atomic package to the experimental line brightness from each charge state. The method is discussed in more detail in Refs. [15,25] for a Maxwell-Boltzmann plasma example. This CSD analysis from spectral line fitting included only transitions whose upper state was predominantly collisionally populated from the ground state. The line intensity fits were performed on the $4f \rightarrow 3d$ emission lines for all the beam plasmas. The $5f \rightarrow 3d$ emission lines were fit for only the $E_{\text{beam}} = 4.54$ and 3.53 keV plasmas. For the $E_{\text{beam}} = 2.66$ and 2.92 keV plasmas, the $5f \rightarrow 3d$ emission lines were not collisionally excited, were very weak, and were not fit to infer a CSD. Sample $5f \rightarrow 3d$ and $4f \rightarrow 3d$ emission spectra recorded by the crystal spectrometer are given in Figs. 1 and 2 for the $E_{\text{beam}} = 3.53$ and 2.92 keV plasmas, respectively. The $4f_{7/2} \rightarrow 3d_{5/2}$, $4f_{5/2} \rightarrow 3d_{3/2}$, $5f_{7/2} \rightarrow 3d_{5/2}$, and $5f_{5/2} \rightarrow 3d_{3/2}$ emission features are clearly seen for the Ni-like (Au^{51+}) to Se-like Au (Au^{45+}) ionization states.

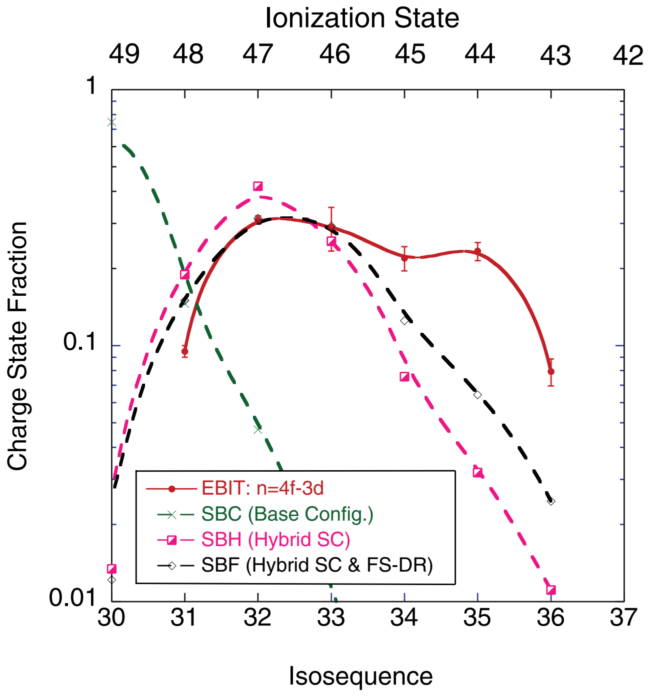

FIG. 7. (Color online) Comparison of the Au charge state distribution at 2.66 keV determined from from the $4f \rightarrow 3d$ transitions measured from the EBIT plasma and simulations from SCRAM.

In the second method, the CSD was determined from the Au radiative recombination emission recorded by the XRS. The RR spectrum is given in Ref. [25] for the $E_{\text{beam}} = 4.54$ keV plasma and shown in Fig. 3 for the 3.53 keV plasma. For the 4.54 keV plasma, the recombination of Ni → Cu, Cu → Zn, Zn → Ga, Ga → Ge, and Ge → As were seen from the continuum into the $n = 4s, 4p_{1/2}, 4p_{3/2}, 4d$, and $4f$ sublevels. Unlike in a Maxwellian plasma, RR x-rays in a monoenergetic electron beam form distinct, resolved features. The RR features appear as lines with widths equal to the FWHM of the Gaussian electron beam energy distribution, which was about 50 eV. The energy of the "line" is equal to the energy of recombination from the continuum into the final state. For a given beam energy, the GRASP calculations provide accurate cross sections for each of the free-bound electron captures and the energies of the emitted photons. The RR intensity is proportional to the fractional ion density, the electron density, and the capture cross section. For a given ion (e.g., Ni-like Au), a synthetic spectrum is generated by using the GRASP cross sections and photon energies assuming Gaussian spectral features. These synthetic spectra generated for each isosequence were fit to the recorded spectra. The Gaussian width and the relative intensity of each isosequence was allowed to vary in the curve fitting routine. The photon energies were kept fixed. The resulting intensities of each isoelectronic sequence yields the CSD for that plasma condition. The experimentally inferred CSDs from the RR emission were determined for the $E_{\text{beam}} =$ 2.92, 3.53, and 4.54 keV beam plasmas. The XRS was not available for the $E_{\text{beam}} = 2.66$ keV beam plasma, so no CSD is available.

The inferred CSDs from both the spectral fits to the RR and the CE emission are shown in Figs. 4, 5, 6, and 7 for the each of the $E_{\text{beam}} = 4.54$, 3.53, 2.92, and 2.66 keV beam plasmas, respectively. In the beam conditions where both CE and RR spectra were taken, the experimentally inferred CSDs from the different methods were very consistent in both the average charge state values $\langle q \rangle$ and the charge state distributions. The values for $\langle q \rangle$ are summarized in Table I. The charge state distributions from all the experimental conditions are summarized in Tables II to IV. For the $E_{\text{beam}} = 4.54$ keV plasma, the $\langle q \rangle$ from the CE spectral fits is 50.6 ± 0.9 and is consistent with the $\langle q \rangle$ of 50.5 ± 1.0 from the RR features. For the $E_{\text{beam}} = 3.53$ keV plasma the same is also true: The

TABLE II. Measured and calculated CSD for EBIT plasmas with $E_{\mathrm{beam}} = 4.54$ keV.

Charge State	Isosequence	$5f \rightarrow 3d$	$4f \rightarrow 3d$	Average	Radiative Recombination	SCRAM (Base Config) SBC	SCRAM (Hybrid SC) SBH	SCRAM (Hybrid SC + FS-DR) SBF
Au^{52+}	Co					0.257	0.114	0.0976
Au^{51+}	Ni	0.69 ± 0.03	0.69 ± 0.02	0.69 ± 0.02	0.60 ± 0.04	0.686	0.755	0.771
Au^{50+}	Cu	0.26 ± 0.02	0.26 ± 0.01	0.26 ± 0.01	0.32 ± 0.02	0.0548	0.0945	0.108
Au^{49+}	Zn	0.056 ± 0.01	0.037 ± 0.004	0.048 ± 0.005	0.069 ± 0.004	0.002 69	0.006 60	0.0111
Au^{48+}	Ga				0.0076 ± 0.0004	1.04×10^{-4}	2.26×10^{-4}	3.42×10^{-4}
Au^{47+}	Ge					3.633×10^{-6}	1.33×10^{-4}	6.69×10^{-6}

$\langle q \rangle$ from the CE line analysis is 49.8 ± 0.8 and is very close to the $\langle q \rangle$ of 49.4 ± 0.3 for the RR spectral fitting analysis.

These experimentally inferred CSDs are consistent with the ionization potentials (I_P) predicted by Scofield [39]. Since the Ni-like Au ion has a closed $3d$ shell, its I_P of 4.89 keV is much greater than the 2.99 keV I_P of Cu-like Au. With a beam energy of 4.54 keV, which lies just below the Ni-like $I_P(\mathrm{Au}^{51+})$ and far from the Cu-like $I_P(\mathrm{Au}^{50+})$, the highest-fraction charge state should be Au^{51+} with little else. This agrees with the measured $\langle q \rangle$ of 50.6 ± 0.9. With a beam energy of 3.53, the fraction of Au^{51+} should be reduced in favor of Au^{50+}, which is consistent with the experiment. The lowest beam energy, 2.66 keV, is between the $I_P(\mathrm{Au}^{47+})$ at 2.65 keV and the $I_P(\mathrm{Au}^{46+})$ at 2.45 keV. The dominant ionization state in the monoenergetic beam plasmas should thus be Ge-like, which is consistent with the experimental $\langle q \rangle$ of 46.5 ± 0.8.

V. COMPARISON WITH MODEL CALCULATIONS

The challenge posed by the unambiguous experimentally inferred CSDs in these well-characterized monoenergetic EBIT plasmas has been to accurately calculate the CSD with a collisional-radiative model. In previous work [24], HULLAC was used to calculate only the collisionally excited line features for each of the recorded charge states. The HULLAC atomic physics package was unable to properly reproduce the experimentally inferred CSDs. The total spectra could only be reproduced assuming the experimental CSD. The inability to model the CSD was not a deficiency with the HULLAC atomic code; rather, computational constraints prevented inclusion of the high-n levels required to engage all the DR resonances at these plasma conditions. The HULLAC calculations included collisional excitation, excitation-autoionization, radiative recombination, and dielectronic recombination, but the maximum level was restricted to $n \leqslant 7$, which is too low to adequately represent DR. It is, however, high enough to correctly calculate the collisionally excited line emission.

The extent of the modeled atomic structure matters because dielectronic recombination is a resonant capture process: the electron energy needed for a capture plus the energy gained in recombining from the continuum to the higher-level state must be equal to the energy needed to excite the low-lying electron into the excited state. For a Maxwellian distribution plasma a large set of resonances are satisfied simultaneously. For a given monoenergetic beam energy, only a small set of capture levels are resonant. Yet, even in this case, there may be many levels that meet the resonance condition, since the energy spectrum of doubly excited states at high n can be densely populated, with energy differences between fine-structure levels much less than the energy spread of the beam. To calculate the CSD of a beam plasma correctly, the correct dielectronic capture levels must be included. For the present beam plasmas, the DR process is resonant with the beam energies only for high-n doubly excited states with $(n,n') = (6\text{–}9, 8\text{–}20)$.

Presented here are three different SCRAM calculations of CSDs for the EBIT monoenergetic beam plasmas. The first calculation includes only levels from low-lying states with $n \leqslant 7$. These are labeled as "SCRAM (Base Configuration)," or SBC. These are consistent with the previous HULLAC calculations. As can be seen in Figs. 4, 5, 6, and 7, the SBC models do not provide a good charge state distribution for the beam plasmas. The calculated CSDs for the all the beam plasmas are significantly more ionized than those inferred from the experiment. These calculations tend to put most of the

TABLE III. Measured and calculated CSD for EBIT plasmas with $E_{\mathrm{beam}} = 3.53$ keV.

Charge State	Isosequence	$5f \rightarrow 3d$	$4f \rightarrow 3d$	Average	Radiative Recombination	SCRAM (Base Config.) SBC	SCRAM (Hybrid SC) SBH	SCRAM (Hybrid SC + FS-DR) SBF
Au^{52+}	Co					1.03×10^{-9}	1.63×10^{-3}	0.001 99
Au^{51+}	Ni	0.20 ± 0.03	0.20 ± 0.01	0.20 ± 0.02	0.16 ± 0.003	0.778	0.348	0.260
Au^{50+}	Cu	0.34 ± 0.02	0.36 ± 0.02	0.35 ± 0.02	0.33 ± 0.01	0.182	0.365	0.386
Au^{49+}	Zn	0.32 ± 0.02	0.30 ± 0.01	0.30 ± 0.01	0.29 ± 0.01	0.0345	0.214	0.231
Au^{48+}	Ga	0.10 ± 0.02	0.10 ± 0.01	0.10 ± 0.01	0.14 ± 0.003	0.003 66	0.0620	0.102
Au^{47+}	Ge	0.038 ± 0.007	0.032 ± 0.007	0.035 ± 0.005	0.075 ± 0.002	4.91×10^{-4}	8.43×10^{-3}	0.0178
Au^{46+}	As					2.16×10^{-4}	7.59×10^{-4}	0.001 86

TABLE IV. Measured and calculated CSD for EBIT plasmas with $E_{\text{beam}} = 2.92$ keV.

Charge State	Isosequence	$4f \rightarrow 3d$	Radiative Recombination	SCRAM (Base Config.) SBC	SCRAM (Hybrid SC) SBH	SCRAM (Hybrid SC + FS-DR) SBF
Au^{51+}	Ni	0.0043 ± 0.002		0.166	0.002 78	1.59×10^{-3}
Au^{50+}	Cu	0.046 ± 0.01	0.062 ± 0.005	0.470	0.0510	0.005 56
Au^{49+}	Zn	0.13 ± 0.02	0.13 ± 0.01	0.198	0.195	0.202
Au^{48+}	Ga	0.24 ± 0.03	0.22 ± 0.02	0.137	0.393	0.397
Au^{47+}	Ge	0.25 ± 0.03	0.23 ± 0.02	0.0243	0.261	0.249
Au^{46+}	As	0.20 ± 0.04	0.20 ± 0.02	0.001 97	0.0829	0.0814
Au^{45+}	Se	0.14 ± 0.04	0.099 ± 0.007	8.59×10^{-5}	0.0120	0.011 381
Au^{44+}	Br	0.057 ± 0.01	0.057 ± 0.004	3.35×10^{-6}	0.001 11	1.62×10^{-3}
Au^{43+}	Kr			1.72×10^{-7}	6.25×10^{-5}	2.95×10^{-4}

charge state distribution into the ions that are closest to the closed shells (e.g., Ni-like).

The second set of calculations is also performed with SCRAM, but it uses the extended hybrid-structure model that includes broadened hydrogenic SCs for doubly excited states up to $(n,n') = (10,20)$. The multiply excited SCs have widths of several hundred eV, which is much broader than the width of the electron beam. In this model, the dielectronic capture cross section into an SC is not represented as a δ function that samples some portion of the beam, as it is for the fine-structure levels and configurations in the base configuration (SBC) model. Rather, the beam is treated as a δ function and the dielectronic capture cross section into an SC is modulated by a Gaussian function representing the statistical spread of levels within that SC. Thus the beam can be resonant with multiple SCs at once and, since the energy separations of the SCs are smaller than their widths, the beams of the present experiments are always resonant with one or more SCs and the DR process dominates over RR. Although the high-lying SCs have very small populations, they also contribute to the ionization rates through excitation followed by autoionization. To prevent an overestimation of the EA flux from SCs that contain both autoionizing and nonautoionizing states (i.e., SCs whose widths are larger than their energies above the ionization limit), a factor representing the population of levels within the SCs that are above the ionization potential is folded into the Auger rates. (This is the $f_{\text{Aug}}^{\Delta n=0}$ factor described in Ref. [30], but it is applied to all SCs rather than just to those with $\Delta n = 0$.) This factor is an important lever on the calculated CSDs, since it depends on the internal distribution of population within the hydrogenic SC. We assume this distribution to be Boltzmann at some effective temperature T_{eff}. Since it is not obvious what value T_{eff} should take in a beam plasma, we have tested its influence at values between 10% and 100% of the beam energy. In general, higher values of T_{eff} lead to more ionized CSDs due to increased EA rates, and midshell ions are more sensitive to variations in T_{eff}. The figures and tables below give results only for $T_{\text{eff}} = E_{\text{beam}}$ and are labeled as "SCRAM (Hybrid SC)," or SBH.

The third set of CSD calculations includes all of the configurations in the extended hybrid-structure model SBH but replaces a portion of the doubly excited hydrogenic SCs with a select set of detailed states for the more important dielectronic capture channels. Thus, this model will have more accurate dielectronic recombination rates (Auger rates from FAC rather than hydrogenic) for a subset of the DR channels. These calculations are designated as "SCRAM (Hybrid SC + FS-DR)," or SBF. The selected dielectronic states were the $3d^k 6fnl$ ($7 \leqslant n \leqslant 9$) for $E_{\text{beam}} = 2.92$ keV, $3d^k 6fnl$ ($8 \leqslant n \leqslant 15$) for $E_{\text{beam}} = 3.63$ keV, and $3d^k 12fnl$ ($16 \leqslant n \leqslant 18$) for $E_{\text{beam}} = 4.54$ keV. The variable k is 9 for Cu-like Au, 10 for Zn-like Au, etc. For the $E_{\text{beam}} = 2.92$ and 2.66 keV plasmas, the As to Kr isoelectronic-sequence models became too large and computationally prohibitive and did not include

TABLE V. Measured and calculated CSD for EBIT plasmas with $E_{\text{beam}} = 2.66$ keV.

Charge State	Isosequence	$4f \rightarrow 3d$	SCRAM (Base Config.) SBC	SCRAM (Hybrid SC) SBH	SCRAM (Hybrid SC + FS-DR) SBF
Au^{50+}	Ni		1.85×10^{-3}	8.22×10^{-6}	9.66×10^{-5}
Au^{51+}	Cu		0.0455	5.38×10^{-4}	0.0102
Au^{52+}	Zn		0.748	0.0134	0.0119
Au^{53+}	Ga	0.063 ± 0.005	0.146	0.190	0.143
Au^{54+}	Ge	0.31 ± 0.01	0.0470	0.419	0.329
Au^{55+}	As	0.29 ± 0.06	0.009 97	0.256	0.343
Au^{56+}	Se	0.22 ± 0.02	8.91×10^{-4}	0.0756	0.118
Au^{57+}	Br	0.23 ± 0.05	6.47×10^{-5}	0.0319	0.0311
Au^{58+}	Kr	0.079 ± 0.01	4.02×10^{-6}	0.0111	0.0115

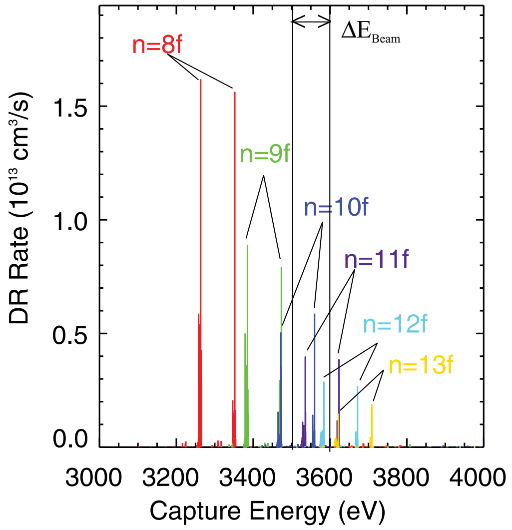

FIG. 8. (Color online) Dielectric capture rate vs capture energy (eV) for $3d6fnf$ with $8 \leqslant n \leqslant 13$ for Ni-like Au into Cu-like Au in the $E_{\mathrm{beam}} = 3.53$ keV monoenergetic beam EBIT plasma.

the high-n DR states. The dielectronic capture rates into these states as a function of capture energy are shown in Figs. 8 and 9 for $3d6fnf$ with $8 \leqslant n \leqslant 13$ for Ni-like Au into Cu-like Au and with $11 \leqslant n \leqslant 15$ for Zn-like Au into Ga-like Au in the $E_{\mathrm{beam}} = 3.53$ keV monoenergetic beam plasma. The SBF calculations are generally a slightly better match to the data than SBH, suggesting that accuracy in the DR and Auger rates is important in addition to completeness.

Including the DR states in both the SBH and the SBF calculations significantly improves the predicted CSD. The CSDs for the two higher beam energies match the experimentally inferred CSDs reasonably well, and the calculated CSDs for the $E_{\mathrm{beam}} = 2.92$ and 2.66 keV condition are a significant improvement from the SBC model, which does not include the higher n DR states. The worst agreement of the CSD calculations are for the lowest-energy $E_{\mathrm{beam}} = 2.66$ keV condition, for which the SBF and SBH models still predict the plasma to be slightly over ionized, with a dominant charge state in Ge-like Au. However, we note that, when the SBH model is run using an effective temperature that is 10% of the beam energy, the EA rates through the supplemental SCs are reduced and the predictions are substantially under ionized, with a dominant charge state below Kr-like Au. It is thus likely that some value of T_{eff} could reproduce the measured data for each beam energy.

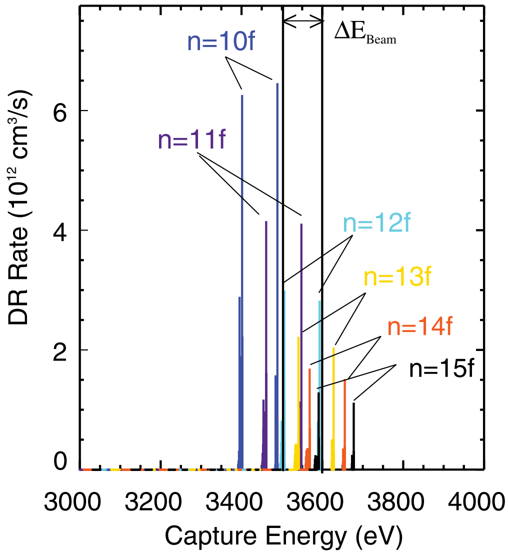

FIG. 9. (Color online) Dielectric capture rate vs capture energy (eV) for $3d6fnf$ with $11 \leqslant n \leqslant 15$ for Zn-like Au into Ga-like Au in the $E_{\mathrm{beam}} = 3.53$ keV monoenergetic beam EBIT plasma.

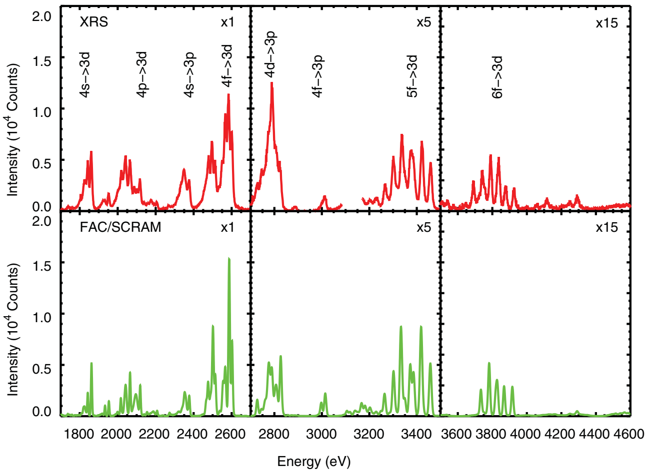

FIG. 10. (Color online) Photometrically calibrated XRS spectrum in the EBIT-I plasma (top) and synthetic SCRAM-FAC spectrum (bottom) at a beam energy of 3.55 keV. Stabilizing transitions from the DR process with energies above 3.55 keV are shown in the rightmost panels.

In addition to its critical role in determining the CSD, the DR capture process results in a doubly excited state that can undergo a stabilizing radiative transition to the ground configuration. Any model that calculates the measured CSD by correctly modeling the DR processes must also predict these stabilizing transitions. Figure 10 shows the XRS spectrum from the $E_{\mathrm{beam}} = 3.53$ keV plasma [24] from 1.8–4.8 keV and a SBF calculation for the same EBIT conditions. The SBF calculation calculates the entire spectral range quite well. The emission in lines in the experimental spectrum above 3.6 keV cannot be collisionally fed since they have energies above the energy of the beam. These lines are $3d^k6fnl \rightarrow 3d^{k+1}nl$ DR stabilizing transitions. We note that, although the previous HULLAC calculations [24] accurately reproduced the CE line emission below photon energies 3.6 keV using the experimentally inferred CSD, the stabilizing transitions were absent from the HULLAC spectrum. The SBF model correctly reproduces not only the experimental CSD but also the x-ray spectrum, including stabilizing transitions

VI. CONCLUSION

We present a systematic study of the charge state distributions of Au plasmas created in the Livermore EBITs. The plasmas had monoenergetic beams with $E_{\mathrm{beam}} = 4.54$, 3.53, 2.92, and 2.66 keV. The x-ray emission from the $5f \rightarrow 3d$ and $4f \rightarrow 3d$ transitions and radiative recombination emission from Au were fit with line emission calculations from HULLAC and RR calculations from GRASP to infer the charge state distributions. The four beam plasmas were modeled using the hybrid-structure SCRAM collisional-radiative model, which is based on atomic data from the FAC and supplemented by hydrogenic superconfigurations. Several variations on the atomic structure included in the models were tested to assess the importance of high-n dielectronic recombination channels, which are resonant with the electron beams for ($8 \leqslant n \leqslant 20$). Only models with extensive atomic structure that included such channels were able to approach the measured data, matching both the inferred CSDs and measured x-ray spectra, including stabilizing transitions associated with the DR process. The performance of these models is a significant improvement in the predictive capabilities of NLTE codes applied to beam plasmas. The present work underscores the importance of both accurate dielectronic recombination rates and extensive, statistically complete energy level structure in collisional-radiative atomic models.

ACKNOWLEDGMENTS

This work was done under the auspices of the US Department of Energy by Lawrence Livermore National Laboratory under Contract No. DE-AC52-07NA27344. Sandia is a multiprogram laboratory operated by Sandia Corporation, a Lockheed Martin Company, for the United States Department of Energy under contract DE-AC04-94AL85000.

[1] K. L. Wong, P. T. Springer, J. H. Hammer, C. A. Iglesias, A. L. Osterheld, M. E. Foord, H. C. Bruns, and J. A. Emig, Phys. Rev. Lett. **80**, 2334 (1998).
[2] A. L. Velikovich, J. Davis, V. I. Oreshkin, J. P. Apruzese, R. Q. Clark, J. W. Thornhill, and L. I. Rudakov, Phys. Plasmas **8**, 4509 (2001).
[3] C. De Michelis and M. Mattioli, Rep. Prog. Phys. **47**, 1233 (1984).
[4] J. E. Rice, J. L. Terry, K. B. Fournier, M. A. Graf, M. Finkenthal, M. J. May, E. S. Marmar, W. H. Goldstein, and A. E. Hubbard, J. Phys. B **29**, 2191 (1996).
[5] J. C. Raymond and N. C. Brickhouse, Astrophys. Space Sci. **237**, 321 (1996).
[6] H. R. Griem, Phys. Fluids B **4**, 2346 (1992).
[7] J. Lindl, Phys. Plasmas **2**, 3933 (1995).
[8] R. W. Lee, J. K. Nash, and Y. Ralchenko, J. Quant. Spectrosc. Radiat. Transfer **58**, 737 (1997).
[9] C. Bowen, A. Decoster, C. J. Fontes, K. B. Fournier, O. Peyrusse, and Yu. V. Ralchenko, J. Quant. Spectrosc. Radiat. Transfer **81**, 71 (2003).
[10] C. Bowen, R. W. Lee, and Y. Ralchenko, J. Quant. Spectrosc. Radiat. Transfer **99**, 102 (2006).
[11] J. G. Rubiano, R. Florido, C. Bowen, R. W. Lee, and Yu. Ralchenko, High Energy Density Physics **3**, 225 (2007).
[12] C. J. Fontes, J. Abdallah Jr., C. Bowen, R. W. Lee, and Yu. Ralchenko, High Energy Density Physics **5**, 15 (2009).
[13] M. E. Foord, S. H. Glenzer, R. S. Thoe, K. L. Wong, K. B. Fournier, B. G. Wilson, and P. T. Springer, Phys. Rev. Lett. **85**, 992 (2000).
[14] S. H. Glenzer, K. B. Fournier, B. G. Wilson, R. W. Lee, and L. J. Suter, Phys. Rev. Lett. **87**, 045002 (2001).
[15] K. L. Wong, M. J. May, P. Beiersdorfer, K. B. Fournier, B. Wilson, G. V. Brown, P. Springer, P. A. Neill, and C. L. Harris, Phys. Rev. Lett. **90**, 235001 (2003).
[16] R. F. Heeter, S. B. Hansen, P. Beiersdorfer M. E. Foord, K. B. Fournier, D. H. Froula, A. J. Mackinnon, M. J. May, M. B. Schneider, and B. K. F. Young, *Proceedings of Atomic Processes in Plasmas 2004*, edited by J. S. Cohen, S. Mazevet, and D. P. Kilcrease (2004), p. 103.
[17] R. F. Heeter, S. B. Hansen, K. B. Fournier, M. E. Foord, D. H. Froula, A. J. Mackinnon, M. J. May, M. B. Schneider, and B. K. F. Young, Phys. Rev. Lett. **99**, 195001 (2007).
[18] B. G. Wilson *et al.*, *Radiative Properties of Hot Dense Matter*, edited by W. Goldstein, C. Hooper, J. Gauthier, J. Seely, and R. Lee (World Scientific, Singapore, 1991).
[19] T. R. Boehly *et al.*, Rev. Sci. Instrum. **66**, 508 (1995).
[20] S. B. Hansen, J. Bauche, C. Bauche-Arnoult, and M. F. Gu, High Energy Density Physics **3**, 109 (2007).
[21] Non-Local Thermodynamic Equalibrium 6 (NLTE6) Proceedings in Rad. Prop. of Hot Dense Matter, 2011.
[22] M. A. Levine, R. E. Marrs, J. R. Henderson, D. A. Knapp, and M. B. Schneider, Phys. Scr. **22**, 157 (1988).
[23] R. Marrs, P. Beiersdorfer, and D. Schneider, Phys. Today **47**, 27 (1994).
[24] M. J. May, K. B. Fournier, P. Beiersdorfer, H. Chen, and K. L. Wong, Phys. Rev. E **68**, 036402 (2003).
[25] M. J. May, P. Beiersdorfer, M. Schneider, S. Terracol, K. L. Wong, K. Fournier, B. Wilson, J. H. Scofield, K. J. Reed, G. Brown, F. S. Porter, R. Kelly, C. A. Kilbourne, and K. R. Boyce, *Proceedings of Atomic Processes in Plasmas 2004*, edited by J. S. Cohen, S. Mazevet, and D. P. Kilcrease (2004), p. 61.
[26] A. Bar-Shalom, M. Klapisch, and J. Oreg, J. Quant. Spectrosc. Radiat. Transfer **71**, 169 (2001).
[27] F. A. Parpia, C. F. Fischer, and I. P Grant, Comput. Phys. Commun. **94**, 249 (1996).
[28] M. F. Gu, Astrophys. J. **582**, 1241 (2003).
[29] M. F. Gu, Can. J. Phys. **86**, 675 (2008).
[30] S. B. Hansen, J. Bauche, and C. Bauche-Arnoult, High Energy Density Physics **7**, 27 (2011).
[31] G. V. Brown, P. Beiersdorfer, and K. Widmann, Rev. Sci. Instrum. **70**, 280 (1999).
[32] P. Beiersdorfer, G. V. Brown, R. Goddard, and B. J. Wargelin, Rev. Sci. Instrum. **75**, 3720 (2004).
[33] P. Beiersdorfer, G. V. Brown, L. Hildebrand, K. L. Wong, and R. Ali, Rev. Sci. Instrum. **72**, 508 (2001).
[34] F. S. Porter *et al.*, Proc. SPIE **4140**, 407 (2000).
[35] R. L. Kelly *et al.*, Proc. SPIE **3765**, 114 (1999).
[36] S. B. Hansen, Can. J. Phys. **89**, 633 (2011).
[37] F. B. Rosmej, Europhys. Lett. **76**, 1081 (2006).
[38] H. A. Scott and S. B. Hansen, High Energy Density Physics **6**, 39 (2010).
[39] J. H. Scofield, Phys. Rev. A **40**, 3054 (1989).